

Three-dimensional discontinuous Galerkin based high-order gas-kinetic scheme and GPU implementation

Yuhang Wang^a, Liang Pan^{a,*}

^a*Laboratory of Mathematics and Complex Systems, School of Mathematical Sciences, Beijing Normal University, Beijing, China*

Abstract

In this paper, the discontinuous Galerkin based high-order gas-kinetic schemes (DG-HGKS) are developed for the three-dimensional Euler and Navier-Stokes equations. Different from the traditional discontinuous Galerkin (DG) methods with Riemann solvers, the current method adopts a kinetic evolution process, which is provided by the integral solution of Bhatnagar-Gross-Krook (BGK) model. In the weak formulation of DG method, a time-dependent evolution function is provided, and both inviscid and viscous fluxes can be calculated uniformly. The temporal accuracy is achieved by the two-stage fourth-order discretization, and the second-order gas-kinetic solver is adopted for the fluxes over the cell interface and the fluxes inside a cell. Numerical examples, including accuracy tests and Taylor-Green vortex problem, are presented to validate the efficiency and accuracy of DG-HGKS. Both optimal convergence and super-convergence are achieved by the current scheme. The comparison between DG-HGKS and high-order gas-kinetic scheme with weighted essential non-oscillatory reconstruction (WENO-HGKS) is also given, and the numerical performances are comparable with the approximate number of degree of freedom. To accelerate the computation, the DG-HGKS is implemented with the graphics processing unit (GPU) using compute unified device architecture (CUDA). The obtained results are also compared with those calculated by the central processing units (CPU) code in terms of the computational efficiency. The speedup of GPU code suggests the potential of high-order gas-kinetic schemes for the large scale computation.

Keywords: High-order gas-kinetic scheme (HGKS), discontinuous Galerkin (DG) method, graphics processing unit (GPU).

1. Introduction

The numerical simulation of compressible flows is an important issue for the computational fluid dynamics, and the construction of high-order numerical schemes becomes demanding for the flows with complicated structures, such as shock, vortex, boundary layer

*Corresponding author

Email addresses: hskwyh@outlook.com (Yuhang Wang), panliang@bnu.edu.cn (Liang Pan)

and turbulence. In recent decades, there have been continuous interests and efforts on the development of high-order schemes, including discontinuous Galerkin (DG), spectral volume (SV) [39], spectral difference (SD) [29], flux reconstruction (FR) [21], correction procedure using reconstruction (CPR) [18, 22], essential non-oscillatory (ENO) [20, 37] and weighted essential non-oscillatory (WENO) schemes [28, 25, 7], etc. The DG method was originally introduced by Reed and Hill [35] in the framework of neutron transport. Cockburn and Shu further developed the DG method in a series of papers [12, 15, 13], in which a framework was established to solve the nonlinear time-dependent hyperbolic conservation laws. Inspired by the great success of DG method for the first-order system, a natural choice to solve a second-order system is to convert it into a first-order system by introducing additional variables, and to apply DG method to the first-order system directly. There are mainly two kinds of approaches, i.e., the first Bassi-Rebay (BR1) scheme [1] and local discontinuous Galerkin (LDG) method [14]. To achieve the compactness, the second Bassi-Rebay (BR2) scheme [2] was developed based on BR1 scheme. Recently, based on the direct weak formulation for solutions of parabolic equations, a direct discontinuous Galerkin (DDG) method was introduced to solve the diffusion equation and Navier-Stokes equations [27, 11]. Generally, for the finite volume methods, such as ENO and WENO schemes, a large stencil is often used to achieve high-order accuracy. Due to the selection of large candidate stencils, these methods face problems on the unstructured meshes, especially for the three-dimensional computation. Meanwhile, DG methods achieve the high-order accuracy by reconstructing a piecewise discontinuous polynomial within each cell, and only the immediate neighbors are involved for the update of flow variables. Compared with the WENO-type methods, the DG methods are less robust. The codes eventually blow up due to the spurious oscillation near discontinuities [15, 13]. Many limiters and trouble cell indicators have been introduced to suppress the oscillations in the literatures for DG methods [33, 34].

In the past decades, the gas-kinetic schemes (GKS) have been developed systematically based on the Bhatnagar-Gross-Krook (BGK) model [3, 10] in the finite volume framework, and applied successfully from low speed flows to hypersonic ones [41, 42]. The gas-kinetic scheme presents a gas evolution process from kinetic scale to hydrodynamic scale, where both inviscid and viscous fluxes are recovered from a time-dependent and genuinely multi-dimensional gas distribution function at cell interface. Based on the two-stage fourth-order temporal discretization for Lax-Wendroff type solvers [26, 17], the high-order gas-kinetic schemes (HGKS) have been constructed and applied for the compressible flow simulations [32, 24, 23]. The fourth-order and even higher-order temporal accuracy can be achieved with the implementation of the traditional second-order or third-order GKS evolution model. More importantly, HGKS is as robust as the second-order scheme, and works perfectly from the subsonic to hypersonic viscous heat conducting flows. With the implementation of three-dimensional WENO reconstruction, the two-stage fourth-order gas-kinetic scheme has been successfully implemented in the direct numerical simulation (DNS) for compressible turbulences [8]. To improve the efficiency, a parallel code of HGKS is developed [8], where the two-dimensional domain decomposition and message passing interface (MPI) are used for the implementation of parallel computing. The scalability of MPI code is examined up to 1024 cores on the TianHe-II supercomputer, and the MPI code scales properly with the

number of processors due to the explicit formulation of the algorithm. With the parallel code, the HGKS provides us a powerful tool for the DNS study from the subsonic to supersonic turbulences.

In this paper, a discontinuous Galerkin based high-order gas-kinetic scheme (DG-HGKS) is developed for the compressible Euler and Navier-Stokes equations. Different from the traditional DG methods with Riemann solvers [38], a time-dependent numerical flux is provided by the gas-kinetic flow solver. The DG-HGKS with third-order and fourth-order spatial accuracy is developed with \mathbb{P}_2 and \mathbb{P}_3 elements, where \mathbb{P}_k is the space of polynomials with the sum of degree at most k for the sum of all variables. Meanwhile, the temporal accuracy is achieved by the two-stage fourth-order discretization [26, 32]. In the computations, we mainly concentrate on the smooth flows, and numerical examples are presented to validate the performance of current method. The accuracy tests are presented to validate the optimal convergence and super-convergence for DG scheme with uniform and nonuniform meshes. The Taylor-Green vortex problem is provided to validate the efficiency and accuracy for the nearly incompressible turbulence. As comparison, the numerical results of HGKS with weighted essential non-oscillatory reconstruction (WENO-HGKS) are given as well. As expected, the numerical performances, including the resolution and efficiency, are comparable with the approximate number of degree of freedom for two methods. To accelerate the computation, the DG-HGKS is implemented to run on graphics processing unit (GPU) using compute unified device architecture (CUDA). The computational efficiency using single Nvidia TITAN RTX and Tesla V100 GPU is demonstrated. Obtained results are compared with those obtained by an octa-core Intel i7-9700K CPU in terms of calculation time. Compared with the CPU code, 6x-7x speedup is achieved for TITAN RTX and 10x-11x speedup is achieved for Tesla V100. Due to the explicit formulation of HGKS, the GPU code can be implemented for WENO-HGKS [8] as well. In the future, more challenging compressible flow problems, such as the turbulent channel flows and the flat plate turbulent boundary layer, will be investigated with multiple GPUs.

This paper is organized as follows. In Section 2, the BGK equation and GKS is briefly reviewed. The DG-HGKS is presented in Section 3, and the GPU architecture and code design are given in Section 4. Numerical examples are included in Section 5. The last section is the conclusion.

2. BGK equation and gas-kinetic scheme

The three-dimensional BGK equation [3, 10] can be written as

$$f_t + u f_x + v f_y + w f_z = \frac{g - f}{\tau}, \quad (1)$$

where $\mathbf{u} = (u, v, w)$ is the particle velocity, f is the gas distribution function, g is the three-dimensional Maxwellian distribution and τ is the collision time. The collision term satisfies the compatibility condition

$$\int \frac{g - f}{\tau} \psi d\Xi = 0, \quad (2)$$

where $\psi = (1, u, v, w, \frac{1}{2}(u^2 + v^2 + w^2 + \xi^2))^T$, the internal variables $\xi^2 = \xi_1^2 + \dots + \xi_K^2$, $d\Xi = dudvdwd\xi_1 \dots d\xi_K$, γ is the specific heat ratio and $K = (5 - 3\gamma)/(\gamma - 1)$ is the degrees of freedom for three-dimensional flows. Taking moments of BGK equation Eq.(1), the macroscopic equation can be written as

$$\frac{\partial Q}{\partial t} + \nabla \cdot \mathbf{F}(Q) = 0, \quad (3)$$

where the conservative variables $Q = (\rho, \rho U, \rho V, \rho W, \rho E)^T$ and the fluxes $\mathbf{F}(Q)$ are given by

$$Q = \int \psi f(\mathbf{x}, t, \mathbf{u}, \xi) d\Xi,$$

$$\mathbf{F}(Q) = \int \mathbf{u} \cdot \mathbf{n} \psi f(\mathbf{x}, t, \mathbf{u}, \xi) d\Xi.$$

According to the Chapman-Enskog expansion for BGK equation, the macroscopic governing equations can be derived. In the continuum region, the BGK equation can be rearranged and the gas distribution function can be expanded as

$$f = g - \tau D_{\mathbf{u}} g + \tau D_{\mathbf{u}} (\tau D_{\mathbf{u}}) g - \tau D_{\mathbf{u}} [\tau D_{\mathbf{u}} (\tau D_{\mathbf{u}}) g] + \dots,$$

where $D_{\mathbf{u}} = \frac{\partial}{\partial t} + \mathbf{u} \cdot \nabla$. With the zeroth-order truncation $f = g$, the Euler equations can be obtained. For the first-order truncation

$$f = g - \tau(ug_x + vg_y + wg_z + g_t),$$

the Navier-Stokes equations can be obtained. More details on the derivation of macroscopic equation can be found in [41, 42].

Originally, the high-order gas-kinetic scheme is developed in the finite volume framework. In the following sections, the control volume is hexahedron for simplicity. Integrating Eq.(3) with respect to space, the semi-discretized finite volume scheme can be expressed as

$$\frac{dQ_i}{dt} = -\frac{1}{|\Omega_i|} \sum_{p=1}^6 \iint_{\Sigma_{i_p}} \mathbf{F}(Q, t) d\sigma, \quad (4)$$

where Q_i is the cell averaged conservative value of hexahedral cell Ω_i , $|\Omega_i|$ is the volume of Ω_i , Σ_{i_p} is the quadrilateral common cell interface of Ω_i and its neighboring cell Ω_{i_p} . To achieve the spatial accuracy, the Gaussian quadrature is used for the surface integral of numerical fluxes over the cell interface

$$\iint_{\Sigma_{i_p}} \mathbf{F}(Q, t) d\sigma = \sum_{m_1, m_2} \omega_{m_1, m_2} F_{m_1, m_2}(t) V_{m_1, m_2},$$

where V_{m_1, m_2} is the area of cell interface related to quadrature point. The numerical flux $F_{m_1, m_2}(t)$ at quadrature point \mathbf{x}_{m_1, m_2} in the global coordinate can be given by

$$F_{m_1, m_2}(t) = \int \psi \mathbf{u} \cdot \mathbf{n}_{m_1, m_2} f(\mathbf{x}_{m_1, m_2}, t, \mathbf{u}, \xi) d\Xi.$$

In the computation, the numerical flux at quadrature points is obtained in the local coordinate, and transferred to the global coordinate. In the local coordinate, the gas distribution function is constructed by the integral solution of BGK equation Eq.(1) as follows

$$f(\mathbf{x}_{m_1, m_2}, t, \mathbf{u}, \xi) = \frac{1}{\tau} \int_0^t g(\mathbf{x}', t', \mathbf{u}, \xi) e^{-(t-t')/\tau} dt' + e^{-t/\tau} f_0(-\mathbf{u}t, \xi),$$

where $\mathbf{u} = (u, v, w)$ is the particle velocity in the local coordinate, $\mathbf{x}_{m_1, m_2} = \mathbf{x}' + \mathbf{u}(t - t')$ is the trajectory of particles, f_0 is the initial gas distribution function, and g is the corresponding equilibrium state. With the reconstruction of macroscopic variables, the second-order gas distribution function at the cell interface can be expressed as

$$\begin{aligned} f(\mathbf{x}_{m_1, m_2}, t, \mathbf{u}, \xi) = & (1 - e^{-t/\tau})g_0 + ((t + \tau)e^{-t/\tau} - \tau)(\bar{a}_1 u + \bar{a}_2 v + \bar{a}_3 w)g_0 \\ & + (t - \tau + \tau e^{-t/\tau})\bar{A}g_0 \\ & + e^{-t/\tau}g_r[1 - (\tau + t)(a_1^r u + a_2^r v + a_3^r w) - \tau A^r](1 - H(u)) \\ & + e^{-t/\tau}g_l[1 - (\tau + t)(a_1^l u + a_2^l v + a_3^l w) - \tau A^l]H(u), \end{aligned} \quad (5)$$

where g_l, g_r are the equilibrium states corresponding to the reconstructed variables Q_l, Q_r at both sides of cell interface. The coefficients in Eq.(5) can be obtained by the reconstructed directional derivatives and compatibility condition

$$\langle a_i^k \rangle = \frac{\partial Q_k}{\partial \mathbf{n}_i}, \langle a_1^k u + a_2^k v + a_3^k w + A^k \rangle = 0,$$

where $k = l, r, i = 1, 2, 3$, the spatial derivatives $\frac{\partial Q_k}{\partial \mathbf{n}_i}$ can be determined by spatial reconstruction and $\langle \dots \rangle$ are the moments of the equilibrium g and defined by

$$\langle \dots \rangle = \int g(\dots) \psi d\Xi.$$

To avoid the extra reconstruction, the conservative variables Q_0 and their spatial derivatives for equilibrium part can be given by the compatibility condition Eq.(2)

$$\begin{aligned} Q_0 &= \int_{u>0} \psi g_l d\Xi + \int_{u<0} \psi g_r d\Xi, \\ \frac{\partial Q_0}{\partial \mathbf{n}_i} &= \int_{u>0} \psi a_i^l g_l d\Xi + \int_{u<0} \psi a_i^r g_r d\Xi. \end{aligned}$$

Similarly, the coefficients in Eq.(5) for the equilibrium part can be obtained by

$$\langle \bar{a}_i \rangle = \frac{\partial Q_0}{\partial \mathbf{n}_i}, \quad \langle \bar{a}_1 u + \bar{a}_2 v + \bar{a}_3 w + \bar{A} \rangle = 0.$$

Thus, the gas-distribution function at the cell interface has been fully determined, and more details of the gas-kinetic scheme can be found in [41].

3. Discontinuous Galerkin based gas-kinetic scheme

In this paper, the three-dimensional structured meshes are considered for simplicity. The computational domain Ω is divided into a collection of non-overlap hexahedrons \mathcal{T} , and each cell is denoted as $K_{ijk} = [x_{i-1/2}, x_{i+1/2}] \times [y_{j-1/2}, y_{j+1/2}] \times [z_{k+1/2}, z_{k+1/2}]$, where $i = 1, \dots, N_x$, $j = 1, \dots, N_y$ and $k = 1, \dots, N_z$. To formulate the discontinuous Galerkin method, the following Sobolev space $\mathbf{V}^{k,m}$ is introduced

$$\mathbf{V}_h^{k,m} = \{ \mathbf{v}_h \in [L^2(\Omega)]^m : v_h|_{K_{ijk}} \in V^{k,m} \},$$

where v_h is one component for vector-valued \mathbf{v}_h , $V^{k,m}$ is the space consisting of discontinuous polynomial functions, and the degree equal or less than k and $m = 5$ is the number of components. Multiplying the governing equation Eq.(3) by a test function $\mathbf{W}_h \in \mathbf{V}_h^{k,m}$, integrating over K_{ijk} , and performing an integration by parts, the following weak formulation can be obtained

$$\frac{d}{dt} \int_{K_{ijk}} Q_h \cdot \mathbf{W}_h d\Omega + \sum_{\Gamma \in \partial K_{ijk}} \int_{\Gamma} \mathbf{F}(Q_h, t) \cdot \mathbf{n} \cdot \mathbf{W}_h d\Gamma - \int_{K_{ijk}} \mathbf{F}(Q_h, t) \cdot \nabla \mathbf{W}_h d\Omega = 0, \quad (6)$$

where $Q_h \in \mathbf{V}_h^{k,m}$ is the solution vector and \mathbf{n} is the unit outward normal vector of cell interface. To discretize the weak formulation, two types of space \mathbb{P}_k and \mathbb{Q}_k can be used for three-dimensional flows, where \mathbb{P}_k is the space of polynomials with the sum of degree at most k for the sum of all variables, and \mathbb{Q}_k is the space of tensor-product polynomials of degree at most k in each variable. For the three-dimensional computation, the degrees of freedom is $(k+1)^3$ for \mathbb{Q}_k and $(k+1)(k+2)(k+3)/6$ for \mathbb{P}_k . The space \mathbb{Q}_k contains much more degrees of freedom than \mathbb{P}_k and more computational cost will be introduced, especially for three-dimensional flows. To reduce the memory and improve efficiency, \mathbb{P}_k space is used. For the one-dimensional DG scheme for the linear advection equation, the $(k+1)$ -th order optimal convergence and $(2k+1)$ -th order super-convergence can be obtained for the DG schemes with the \mathbb{P}_k element. The numerical results will show that the optimal convergence and super-convergence can be achieved by DG-HGKS for three-dimensional Euler equations as well.

The three-dimensional Legendre polynomials are chosen as the basis functions of $\mathbf{V}_h^{k,m}$

$$\mathbf{B}_{\mathbf{n}}(\mathbf{x}) = P_{i,n_x}(x)P_{j,n_y}(y)P_{k,n_z}(z),$$

where $\mathbf{n} = (n_x, n_y, n_z)$ is the multi-index, $P_{i,l}(x) = P_l(\xi)$ with $\xi = 2(x - x_i)/\Delta x_i$ and $P_l(\xi)$ is the l th-order Legendre polynomial that are orthogonal on $[-1, 1]$. The time dependent solution vector $Q_h(\mathbf{x}, t)$ is represented by the following expansion

$$Q_h(\mathbf{x}, t) = \sum_{n=1}^N Q_{h,n}(t) \mathbf{B}_n(\mathbf{x}), \quad (7)$$

where $Q_{h,n}(t)$ is the n -th unknown degree of freedom, $n = n_x + n_y + n_z$ and N is the total number of basis functions. Taking $\mathbf{W}_h = \mathbf{B}_n(\mathbf{x})$ in Eq.(6), the DG formulation is equivalent to the following system

$$\frac{d}{dt} \int_{K_{ijk}} Q_h \cdot \mathbf{B}_n d\Omega + \sum_{\Gamma \in \partial K_{ijk}} \int_{\Gamma} \mathbf{F}_b(Q_h, t) \cdot \mathbf{n} \cdot \mathbf{B}_n d\Gamma - \int_{K_{ijk}} \mathbf{F}_v(Q_h, t) \cdot \nabla \mathbf{B}_n d\Omega = 0, \quad (8)$$

where $\mathbf{F}_b(Q_h, t)$ is the numerical flux across the cell interface and $\mathbf{F}_v(Q_h, t)$ is the numerical flux inside each volume. According to the expansion Eq.(7), the DG formulation Eq.(8) leads to a system of ordinary differential equations

$$\frac{dQ_h}{dt} = \mathbf{M}^{-1} \mathcal{R}(Q_h) = \mathcal{L}(Q_h),$$

where each term of the mass matrix $\mathbf{M}_{N \times N}$ is defined by

$$\mathbf{M}_{n_1, n_2} = \int_{K_{ijk}} \mathbf{B}_{n_1} \mathbf{B}_{n_2} d\Omega,$$

and the operator $\mathcal{R}(Q_h)$ is given by

$$\mathcal{R}(Q_h) = - \sum_{\Gamma \in \partial K_{ijk}} \int_{\Gamma} \mathbf{F}_b(Q_h, t) \cdot \mathbf{n} \cdot \mathbf{B}_n dS + \int_{K_{ijk}} \mathbf{F}_v(Q_h, t) \cdot \nabla \mathbf{B}_n d\Omega. \quad (9)$$

The Gaussian quadrature is used for the surface integral

$$\int_{\Gamma} \mathbf{F}_b(\mathbf{U}_h, t) \cdot \mathbf{n} \cdot \mathbf{B}_n dS = \sum_{m_1, m_2} \omega_{m_1, m_2} \mathbf{F}_b(\mathbf{x}_{m_1, m_2}, t) \cdot \mathbf{n} \cdot \mathbf{B}_n(\mathbf{x}_{m_1, m_2}) |\Gamma|, \quad (10)$$

where ω_{m_1, m_2} is the quadrature weight for 2D Gaussian quadrature, $|\Gamma|$ is the area of Γ , and the numerical flux $\mathbf{F}_b(\mathbf{x}_{m_1, m_2}, t)$ can be obtained by taking moments of gas distribution function given by Eq.(5)

$$\mathbf{F}_b(\mathbf{x}_{m_1, m_2}, t) = \int \psi \mathbf{u} \cdot \mathbf{n}_{m_1, m_2} f(\mathbf{x}_{m_1, m_2}, t, \mathbf{u}, \xi) d\Xi.$$

Similarly, the Gaussian quadrature is also used for the volume integral

$$\int_{K_{ijk}} \mathbf{F}_v(Q_h) \cdot \nabla \mathbf{B}_i d\Omega = \sum_{m_1, m_2, m_3} \omega_{m_1, m_2, m_3} \mathbf{F}_v(\mathbf{x}_{m_1, m_2, m_3}, t) \cdot \nabla \mathbf{B}_i(\mathbf{x}_{m_1, m_2, m_3}) |K_{ijk}|, \quad (11)$$

where ω_{m_1, m_2, m_3} is the quadrature weight for 3D Gaussian quadrature, $|K_{ijk}|$ is the volume of K_{ijk} , and the numerical flux $\mathbf{F}_v(\mathbf{x}_{m_1, m_2, m_3}, t)$ can be given by

$$\mathbf{F}_v(\mathbf{x}_{m_1, m_2, m_3}, t) = \int \psi \mathbf{u} \cdot \mathbf{n}_{m_1, m_2, m_3} f(\mathbf{x}_{m_1, m_2, m_3}, t, \mathbf{u}, \xi) d\Xi.$$

Remark 1. *The macroscopic flow variables inside a cell are updated automatically with smooth assumption, and the simplified version of gas distribution function is used*

$$f(\mathbf{x}_{m_1, m_2, m_3}, t, \mathbf{u}, \xi) = g_0(1 - \tau(a_1 u + a_2 v + a_3 w + A) + At), \quad (12)$$

where the coefficients in Eq.(12) can be obtained by the reconstructed directional derivatives and compatibility condition

$$\langle a_i \rangle = \frac{\partial Q}{\partial \mathbf{n}_i}, \langle a_1 u + a_2 v + a_3 w + A \rangle = 0.$$

In the numerical cases, the smooth flow without discontinuities are considered and the collision time takes

$$\tau = \frac{\mu}{p}.$$

For the accuracy tests, the inviscid flows are considered. The collision time τ and viscous coefficient μ take 0, and the gas distribution functions for the surface and volume integrations reduce to

$$f = g_0(1 + At).$$

In this paper, we mainly focus on the smooth flows. For the flows with discontinuities, and the limiters and trouble indicators need to be used, the coupling with the current scheme will be investigated in the future.

Remark 2. *To achieve the spatial accuracy, \mathbb{P}_2 and \mathbb{P}_3 spaces are used. The two-point and three-point Gaussian quadratures are adopted, i.e. For the \mathbb{P}_2 space, 2^2 numerical fluxes are calculated for surface integration Eq.(10) and 2^3 numerical fluxes are calculated for volume integration Eq.(11); For the \mathbb{P}_3 space, 3^2 and 3^3 numerical fluxes are calculated for the surface and volume integrations respectively.*

In the classical numerical methods, the numerical fluxes are usually provided by the approximate or exact Riemann solvers [38], and the Runge-Kutta method is used for temporal

accuracy [19]. A two-stage fourth-order time-accurate discretization was developed for the hyperbolic equations with the generalized Riemann problem (GRP) solver [26, 17] and the gas-kinetic scheme [32]. Consider the following time-dependent equation

$$\frac{dQ}{dt} = \mathcal{L}(Q),$$

with the initial condition at t_n ,

$$Q(t)|_{t=t_n} = Q^n,$$

where $\mathcal{L}(Q) = \mathbf{M}^{-1}\mathcal{R}(Q)$. Introducing an intermediate state at $t^* = t_n + \Delta t/2$,

$$\begin{aligned} Q^* &= Q^n + \frac{1}{2}\Delta t\mathcal{L}(Q^n) + \frac{1}{8}\Delta t^2\mathcal{L}_t(Q^n), \\ Q^{n+1} &= Q^n + \Delta t\mathcal{L}(Q^n) + \frac{1}{6}\Delta t^2(\mathcal{L}_t(Q^n) + 2\mathcal{L}_t(Q^*)). \end{aligned} \quad (13)$$

It can be proved that for hyperbolic equations the two-stage time stepping method Eq.(13) provides a fourth-order time accurate solution for $Q(t)$ at $t = t_n + \Delta t$. To implement the two-stage fourth-order method, the following terms need to be constructed by the Gaussian quadrature point

$$\begin{aligned} &\mathbf{F}_b(Q_h(\mathbf{x}_{m_1, m_2}, t_n)), \partial_t \mathbf{F}_b(Q_h(\mathbf{x}_{m_1, m_2}, t_n)), \\ &\mathbf{F}_v(Q_h(\mathbf{x}_{m_1, m_2, m_3}, t_n)), \partial_t \mathbf{F}_v(Q_h(\mathbf{x}_{m_1, m_2, m_3}, t_n)). \end{aligned}$$

A linear function is used to approximate the time dependent numerical flux

$$\mathbf{F}(Q_h(\mathbf{x}, t)) = \mathbf{F}(Q_h(\mathbf{x}, t_n)) + \partial_t \mathbf{F}(Q_h(\mathbf{x}, t_n))(t - t_n), \quad (14)$$

where the subscripts b, v and indexes for quadrature points are omitted. Integrating Eq.(14) over $[t_n, t_n + \Delta t]$ and $[t_n, t_n + \Delta t/2]$, we have the following two equations

$$\begin{aligned} \mathbf{F}(Q_h(\mathbf{x}, t_n))\Delta t + \frac{1}{2}\partial_t \mathbf{F}(Q_h(\mathbf{x}, t_n))\Delta t^2 &= \int_{t_n}^{t_n+\delta} \mathbf{F}(Q_h(\mathbf{x}, t))dt, \\ \frac{1}{2}\mathbf{F}(Q_h(\mathbf{x}, t_n))\Delta t + \frac{1}{8}\partial_t \mathbf{F}(Q_h(\mathbf{x}, t_n))\Delta t^2 &= \int_{t_n}^{t_n+\delta/2} \mathbf{F}(Q_h(\mathbf{x}, t))dt. \end{aligned}$$

The coefficients can be determined by solving the linear system, and $\mathcal{L}(Q^n)$ and $\mathcal{L}_t(Q^n)$ can be given. Similarly, $\mathcal{L}(Q^*)$ and $\mathcal{L}_t(Q^*)$ can be given at $t = t_n + \Delta/2$. Thus, the DG-HGKS can be implemented.

4. GPU architecture and code design

Graphics processing unit (GPU) is a form of hardware acceleration, which is originally developed for graphics manipulation and is extremely efficient at processing large amounts of data in parallel, such as pixel transformations. Currently, GPU has gained significant popularity in large-scale scientific computations [40]. Due to the different purposes of designed, the architectures of CPU and GPU are different. A central processing unit (CPU) is designed to execute a sequence of tasks quickly, but is limited in the number of threads which are handled in parallel. Meanwhile, a GPU is designed to execute highly-parallel computing tasks, and it may handle thousands of threads at the same time.

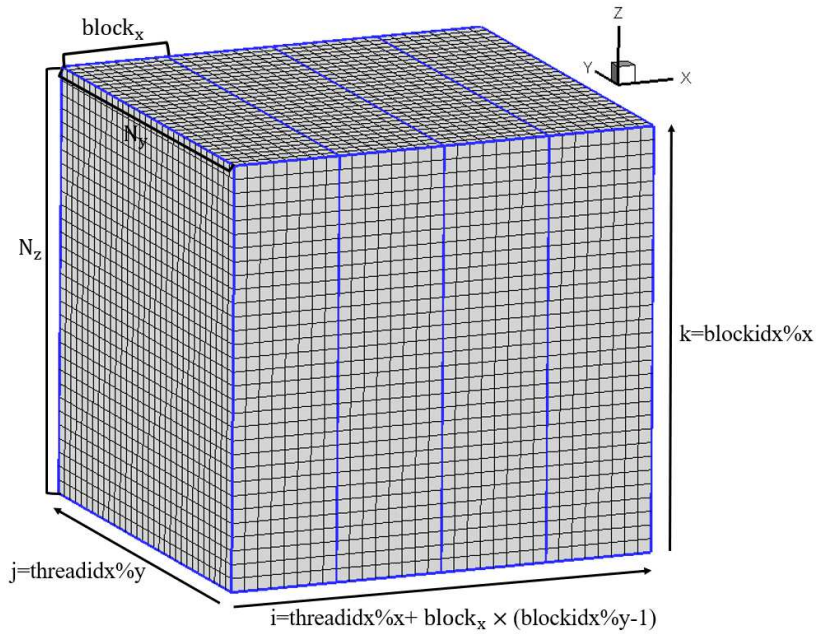


Figure 1: Connection between threads and cells.

	threadidx%x	threadidx%y	blockidx%x	blockidx%y
range of value	[1, block _x]	[1, N _y]	[1, N _z]	[1, N _x /block _x]

Table 1: Range of values for "threadidx" and "blockidx".

In this paper, to accelerate the computation, DG-HKGS is implemented on GPU using CUDA. The way to implement the algorithm in parallel on GPU is using kernels. The kernel is a subroutine, which executes at the same time by many threads on GPU. According to the algorithm of DG-HGKS proposed above, the subroutines of surface integrals for \mathbf{F}_v and $\partial_t \mathbf{F}_v$ in Eq.(10), the volume integrals for \mathbf{F}_b and $\partial_t \mathbf{F}_b$ in Eq.(11) and the update of flow variables Q_h can be implemented parallelly. Therefore, these subroutines can be coded as

kernels. In order to improve the efficiency, \mathbf{F}_v , $\partial_t \mathbf{F}_v$, \mathbf{F}_b , $\partial_t \mathbf{F}_b$ and Q_h are saved as global variables stored in global memory. The code can be expressed with following steps

1. dispatching $Q_h(t_n)$ of K_{ijk} and its neighboring cells from global memory to local at t_n ,
2. computing \mathbf{F}_v , $\partial_t \mathbf{F}_v$ and \mathbf{F}_b , $\partial_t \mathbf{F}_b$, and obtaining $\mathcal{R}(Q_h)$ by Eq.(9) at t_n ,
3. updating $Q_h(t^*)$ of cell K_{ijk} according to Eq.(13),
4. dispatching the updated $Q_h(t^*)$ back to global memory,
5. repeating the procedures above at the intermediate stage t^* .

The CUDA threads are organized into thread blocks, and thread blocks constitute a grid which may be seen as a computational structure on GPUs. In this study, the three-dimensional structured meshes are used, a simple partition of grid is established, which is shown in Figure.1. Assume that the total number of meshes is $N_x \times N_y \times N_z$, and the three-dimensional computational domain is divided into block_x parts in x -direction, where block_x is an integer defined according to tests. The variables "dimGrid" and "dimBlock" are defined to set a two-dimensional grid, which consist of two-dimensional blocks as follows

$$\begin{aligned} \text{dimGrid} &= \text{dim3}(N_z, N_x/\text{block}_x, 1), \\ \text{dimBlock} &= \text{dim3}(\text{block}_x, N_y, 1). \end{aligned}$$

Each thread gets a block index "blockidx" and a thread index "threadidx", where the two variables have two components and the range of values are given in Table.1. It is natural to assign one thread to complete computations of a cell K_{ijk} . The one-to-one correspondence of thread block index and cell index (i, j, k) is given as follows

$$\begin{aligned} i &= \text{threadidx}\%0x + \text{block}_x * (\text{blockidx}\%0y - 1), \\ j &= \text{threadidx}\%0y, \\ k &= \text{blockidx}\%0x. \end{aligned}$$

The Nvidia GPU is consisted of multiple streaming multiprocessors (SMs). Each block of grid is distributed to one SM, and the threads of block are executed in parallel on SM. The executions are implemented automatically by GPU. Thus, the GPU code can be implemented with specifying kernels and grids, and the performance will be tested.

5. Numerical simulation and discussion

5.1. Accuracy tests

For the one-dimensional scalar hyperbolic equation and hyperbolic system, the optimal $(k + 1)$ -th order convergence can be obtained with \mathbb{P}_k elements. For the multidimensional cases, the optimal $(k + 1)$ -th order can be achieved, when the piecewise tensor product polynomials are used, i.e., \mathbb{Q}_k elements. Recently, for the two-dimensional scalar hyperbolic equations, the optimal $(k + 1)$ -th order convergence is proved for \mathbb{P}_k elements on uniform Cartesian meshes [31]. For one-dimensional linear hyperbolic equations, with suitable correction function, the super-convergence [9] can be proved at the downwind points and for

the domain average with quasi-uniform meshes and some suitable initial discretization. This technique was developed to study other kinds of DG methods, such as the local DG method, the direct DG method. Two cases will be provided to test the optimal convergence and super-convergence of DG-HGKS for nonlinear Euler equations. To test the optimal convergence, the L^1 and L^2 errors are calculated, and the definitions are given as follows

$$e_{L^1} = \left(\sum_{\Omega_e \in \mathcal{T}_h} \left(\int_{\Omega_e} |u - u_h| d\Omega \right) \right),$$

$$e_{L^2} = \left(\sum_{\Omega_e \in \mathcal{T}_h} \left(\int_{\Omega_e} |u - u_h|^2 d\Omega \right) \right)^{1/2},$$

where u is the exact solution and u_h is the approximate numerical solution, and Gaussian quadrature is used for the integration. To test super-convergence of DG scheme, the error for the cell averaged value is defined as follows

$$e_c = \left(\sum_{\Omega_e \in \mathcal{T}_h} \left(\int_{\Omega_e} |\bar{u} - \bar{u}_h|^2 d\Omega \right) \right)^{1/2}.$$

where \bar{u} is cell averaged value of exact solution and \bar{u}_h is cell averaged value of numerical solution.

The first case is the advection of density perturbation for the two-dimensional and three-dimensional flows, which are linear problems for accuracy test. For the two-dimensional case, the physical domain is $[0, 2] \times [0, 2]$ and the initial condition is set as follows

$$\rho_0(x, y) = 1 + 0.2 \sin(\pi(x + y)), \quad p_0(x, y) = 1, \quad U_0(x, y) = 1, \quad V_0(x, y) = 1.$$

The periodic boundary conditions are applied at boundaries, and the exact solution is

$$\rho(x, y, t) = 1 + 0.2 \sin(\pi(x + y - t)), \quad p(x, y, t) = 1, \quad U(x, y, t) = 1, \quad V(x, y, t) = 1.$$

This case is tested with uniform and nonuniform meshes. For the uniform meshes, the mesh with $\Delta x = \Delta y = 2/N$ are tested. For the nonuniform mesh, the grid points are given by the following transformation

$$\begin{cases} x = \xi + 0.05 \sin(\pi\xi), \\ y = \eta + 0.05 \sin(\pi\eta). \end{cases}$$

For the three-dimensional case, the physical domain is $[0, 2] \times [0, 2] \times [0, 2]$ and the initial condition is set as follows

$$\rho_0(x, y, z) = 1 + 0.2 \sin(\pi(x + y + z)), \quad p_0(x, y, z) = 1,$$

$$U_0(x, y, z) = 1, \quad V_0(x, y, z) = 1, \quad W_0(x, y, z) = 1.$$

The periodic boundary conditions are applied at boundaries, and the exact solution is

$$\begin{aligned}\rho(x, y, z, t) &= 1 + 0.2 \sin(\pi(x + y + z - t)), \quad p(x, y, z, t) = 1, \\ U(x, y, z, t) &= 1, \quad V(x, y, z, t) = 1, \quad W(x, y, z, t) = 1.\end{aligned}$$

This case is also tested with uniform and nonuniform meshes. For the uniform meshes, the mesh with $\Delta x = \Delta y = \Delta z = 2/N$ are tested. For the nonuniform mesh, the grid point is given by the following transformation

$$\begin{cases} x = \xi + 0.05 \sin(\pi\xi), \\ y = \eta + 0.05 \sin(\pi\eta), \\ z = \zeta + 0.05 \sin(\pi\zeta). \end{cases}$$

In the computation, the \mathbb{P}_2 and \mathbb{P}_3 elements are tested. The L^1 and L^2 errors and orders of accuracy for the two-dimensional problem are given in Table.2, Table.3, Table.4 and Table.5 for both uniform and nonuniform meshes, and the expected $(k + 1)$ -th order of accuracy is observed. For the hyperbolic scalar equation, $(2k + 1)$ -th order super-convergence is expected [9] for the error of cell averaged value. For the current method, the error of cell averaged value and orders of accuracy are also given in Table.2, Table.3, Table.4 and Table.5 for both uniform and nonuniform meshes, and the $2k$ -th order super-convergence is observed for \mathbb{P}_k elements. It might be because the fewer Gaussian quadrature points for Eq.(10) and Eq.(11). The L^1 and L^2 errors and orders of accuracy for the three-dimensional problem are given in Table.6, Table.7, Table.8 and Table.9, and the expected $(k + 1)$ -th order of accuracy are observed as well. Due to the very small time step, the super-convergence for three-dimensional problem is not given. It is also believed that the $2k$ -th order super-convergence can be achieved for \mathbb{P}_k elements.

The second case is the isotropic vortex propagation problem, and it is a non-linear case for accuracy test. The initial condition is given by a mean flow $(\rho, U, V, p) = (1, 1, 1, 1)$. An isotropic vortex is added to the mean flow, i.e., with perturbation in U , V and temperature $T = p/\rho$, and no perturbation in entropy $S = p/\rho^\gamma$. The perturbation is given by

$$(\delta U, \delta V) = \frac{\epsilon}{2\pi} e^{\frac{(1-r^2)}{2}} (-y, x), \quad \delta T = -\frac{(\gamma - 1)\epsilon^2}{8\gamma\pi^2} e^{1-r^2}, \quad \delta S = 0,$$

where $r^2 = x^2 + y^2$ and the vortex strength $\epsilon = 5$. The computational domain is $[0, 10] \times [0, 10]$, and the periodic boundary conditions are imposed on the boundaries in all directions. The exact solution is the perturbation of isotropic vortex which propagates with the velocity $(1, 1)$. In the computation, this case is tested by \mathbb{P}_2 and \mathbb{P}_3 elements, and the uniform mesh with N^2 cells are used. The L^1 and L^2 errors and orders of accuracy are given in Table.10 and Table.11, and the expected $(k + 1)$ -th order of accuracy is observed for \mathbb{P}_k elements. The errors for cell averaged value are given in Table.10 and Table.11, and the $(k + 3/2)$ -th order super-convergence is observed.

In these two cases, the optimal order of accuracy are obtained for both linear and non-

mesh	L^1 error	Order	L^2 error	Order	$e_{u,c}$ error	Order
8^2	1.2632E-02		5.0047E-03		5.6223E-04	
16^2	1.2982E-03	3.2824	5.1162E-04	3.2902	2.4338E-05	4.5299
32^2	1.5215E-04	3.0930	5.9793E-05	3.0970	1.1353E-06	4.4220
64^2	1.8633E-05	3.0296	7.3140E-06	3.0312	6.1540E-08	4.2054

Table 2: Accuracy test: 2D advection of density perturbation for \mathbb{P}_2 element with uniform cells.

mesh	L^1 error	Order	L^2 error	Order	$e_{u,c}$ error	Order
8^2	6.4334E-04		3.1235E-04		4.5650E-06	
16^2	3.8232E-05	4.0727	1.7848E-05	4.1293	4.5357E-08	6.6531
32^2	2.3296E-06	4.0366	1.0881E-06	4.0359	7.0660E-10	6.0043
64^2	1.4433E-07	4.0126	6.7525E-08	4.0102	1.0552E-11	6.0653

Table 3: Accuracy test: 2D advection of density perturbation for \mathbb{P}_3 element with uniform cells.

mesh	L^1 error	Order	L^2 error	Order	$e_{u,c}$ error	Order
8^2	1.3484E-02		5.4209E-03		6.2038E-04	
16^2	1.3756E-03	3.2932	5.4617E-04	3.3111	2.7181E-05	4.5125
32^2	1.6055E-04	3.0989	6.3559E-05	3.1032	1.2526E-06	4.4396
64^2	1.9643E-05	3.0310	7.7662E-06	3.0328	6.6467e-08	4.2361

Table 4: Accuracy test: 2D advection of density perturbation for \mathbb{P}_2 element with nonuniform cells.

mesh	L^1 error	Order	L^2 error	Order	$e_{u,c}$ error	Order
8^2	8.3231E-04		3.6625E-04		6.0414E-06	
16^2	4.4123E-05	4.2375	1.9564E-05	4.2266	8.4484E-08	6.1601
32^2	2.6616E-06	4.0512	1.1505E-06	4.0878	5.8786E-10	7.1671
64^2	1.6712E-07	3.9933	7.0616E-08	4.0262	1.1928E-11	5.6230

Table 5: Accuracy test: 2D advection of density perturbation for \mathbb{P}_3 element with nonuniform cells.

linear problems for \mathbb{P}_k elements for two and three-dimensional nonlinear hyperbolic system. Meanwhile, the super-convergence are also observed for both linear and nonlinear problems. For the nonlinear systems, the error estimates of optimal convergence and super-convergence for \mathbb{P}_k elements are still very challenging for DG schemes, and more studies will be investigated in the future.

mesh	L^1 error	Order	L^2 error	Order
8^3	3.6718E-02		1.4834E-03	
16^3	2.9226E-03	3.6512	1.1441E-03	3.6965
32^3	2.9518E-04	3.3076	1.1712E-04	3.2882
64^3	3.4117E-05	3.1130	1.3830E-05	3.0821

Table 6: Accuracy test: 3D advection of density perturbation for \mathbb{P}_2 element with uniform cells.

mesh	L^1 error	Order	L^2 error	Order
8^3	1.6627E-03		8.9026E-04	
16^3	9.0567E-05	4.1984	5.3092E-05	4.0677
32^3	5.6787E-06	3.9954	3.3471E-06	3.9875
64^3	3.5448E-07	4.0018	2.0974E-07	3.9962

Table 7: Accuracy test: 3D advection of density perturbation for \mathbb{P}_3 element with uniform cells.

mesh	L^1 error	Order	L^2 error	Order
8^3	3.9464E-02		1.6035E-02	
16^3	3.1274E-03	3.6575	1.2335E-03	3.7004
32^3	3.1367E-04	3.3177	1.2516E-04	3.3009
64^3	3.6132E-05	3.1179	1.4737E-05	3.0864

Table 8: Accuracy test: 3D advection of density perturbation for \mathbb{P}_2 element with nonuniform cells.

mesh	L^1 error	Order	L^2 error	Order
8^3	2.1888E-03		1.0100E-03	
16^3	1.0973E-04	4.3181	5.4167E-05	4.2208
32^3	6.7226E-06	4.0288	3.3516E-06	4.0145
64^3	4.1725E-07	4.0100	2.0926E-07	4.0015

Table 9: Accuracy test: 3D advection of density perturbation for \mathbb{P}_3 element with nonuniform cells.

5.2. Efficiency comparison of CPU and GPU

The efficiency comparison of CPU and GPU code is provided with the three-dimensional advection of density perturbation. The CPU code is computed with an octa-core Intel i7-9700 CPU using Intel Fortran compiler with OpenMP directives, while Nvidia TITAN RTX and Nvidia Tesla V100 are used for GPU computation with Nvidia CUDA and NVFOR-

mesh	L^1 error	Order	L^2 error	Order	e_c error	Order
20^2	9.9414E-01		4.7547E-02		2.5500E-04	
40^2	1.2966E-01	2.9387	7.0093E-03	2.7620	1.5981E-05	3.9961
80^2	1.8311E-02	2.8240	1.1796E-03	2.5709	1.4020E-06	3.5107
160^2	2.3769E-03	2.9456	2.0082E-04	2.5544	1.3725E-07	3.3527

Table 10: Accuracy test: isotropic vortex propagation problem for \mathbb{P}_2 element with uniform cells.

mesh	L^1 error	Order	L^2 error	Order	e_c error	Order
20^2	8.7222E-02		4.0368E-03		1.2223E-05	
40^2	3.6128E-03	4.5935	2.0043E-04	4.3320	3.0863E-07	5.3076
80^2	1.9642E-04	4.2011	1.2460E-05	4.0077	1.0386E-08	4.8931
160^2	1.1337E-05	4.1148	8.0350E-07	3.9549	4.1164E-10	4.6572

Table 11: Accuracy test: isotropic vortex propagation problem for \mathbb{P}_3 element with uniform cells.

TRAN compiler. The detailed parameters of GPU and CPU are given in Table.12. Double precision is used in computation. The number of the uniform meshes used for tests is from 16^3 to 128^3 , and the computational times are recorded at $t = 2$. The computational times and speedups for the DG-HGKS with different meshes are given in Table.13, where speedup is defined as

$$\text{speedup} = \frac{\text{computational time of CPU}}{\text{computational time of GPU}}.$$

Theoretically, the total computation amount increases by a factor of 16, when the number of cells doubles in every direction. As expected, the computational time for the parallel CPU code increase by the same factor approximately. The GPU computational time increases by a factor less than 16 for coarse meshes, and the factor reaches 16 for the finer meshes. The speedup increases when the number of cells increases, and reaches an almost constant value. Compared with the CPU code, 6x-7x speedup is achieved for TITAN RTX and 10x-11x speedup is achieved for Tesla V100. In the future, the code of HGKS will be developed with multiple GPUs, and more challenging problems for compressible flows will be investigated.

5.3. Taylor-Green vortex

The Taylor-Green vortex is a classical problem in fluid dynamics developed to study vortex dynamics, turbulent transition, turbulent decay and energy dissipation process [5]. It has become an excellent case for the evaluation of turbulent flow simulation methodologies, and been used by many authors for high-order method validation [6, 16]. In the previous study [24], this problem is provided to test the performance of WENO-HGKS up to 1024^3 uniform cells for the direct numerical simulation (DNS) of nearly incompressible turbulent flows, and the performance demonstrated the capability of HGKS as a powerful DNS tool.

	Intel i7-9700 CPU	Nvidia TITAN RTX	Nvidia Tesla V100
clock rate	3.0 GHz	1.77 GHz	1.53 GHz
stream multiprocessor	-	72	80
FP64 core per SM	-	2	32
double precision	384 GFLOPS	509.8 GFLOPS	7.834 TFLOPS

Table 12: Efficiency comparison: the detailed parameters of GPU and CPU.

method	CPU	GPU (TITAN RTX)	Speedup	GPU (Tesla V100)	Speedup
16^3	28s	12s	2.3	4s	7.0
32^3	394s	82s	4.8	39s	10.1
64^3	5522s	848s	6.5	499s	11.1
128^3	85556s	12692s	6.7	7927s	10.8

Table 13: Efficiency comparison: the computational time and speedup for GPU and CPU computation.

In the computation, the DG-HGKS with \mathbb{P}_2 and \mathbb{P}_3 elements are tested, and the uniform meshes with 32^3 , 64^3 and 96^3 cells are used. As comparison, the results of WENO-HGKS are also provided as benchmark, where the uniform meshes with 64^3 , 128^3 and 256^3 cells are used and fifth-order WENO scheme with linear weights is adopted.

The flow is computed within a periodic square box defined as $-\pi L \leq x, y, z \leq \pi L$. With a uniform temperature, the initial condition is given by

$$\begin{aligned}
U &= V_0 \sin\left(\frac{x}{L}\right) \cos\left(\frac{y}{L}\right) \cos\left(\frac{z}{L}\right), \\
V &= -V_0 \cos\left(\frac{x}{L}\right) \sin\left(\frac{y}{L}\right) \cos\left(\frac{z}{L}\right), \\
W &= 0, \\
p &= p_0 + \frac{\rho_0 V_0^2}{16} \left(\cos\left(\frac{2x}{L}\right) + \cos\left(\frac{2y}{L}\right) \right) \left(\cos\left(\frac{2z}{L}\right) + 2 \right),
\end{aligned}$$

where $L = 1$, $V_0 = 1$, $\rho_0 = 1$, and the Mach number takes $M_0 = V_0/c_0 = 0.1$, where c_0 is the sound speed. The characteristic convective time $t_c = L/V_0$, the fluid is a perfect gas with $\gamma = 1.4$, Prandtl number is $Pr = 1$ and Reynolds number $Re = 1600$. To test the performance of high-order schemes, several diagnostic quantities are computed from the flow as it evolves in time. This case is given by a simple construction, and contains several key physical processes including vortex stretching, interaction and dilatation effects. As time evolves, the vortex roll-up, stretch and interact, eventually breaking down into turbulence. The iso-surface of the second invariant of velocity gradient tensor Q_v colored by velocity magnitude at $t = 2.5, 5, 7.5$ and 10 with 96^3 cells for \mathbb{P}_3 element are shown in Figure.2. At

the earliest time, the flow behaves inviscidly as the vortex begin to evolve and roll-up. At $t = 10$, the coherent structures breakdown.

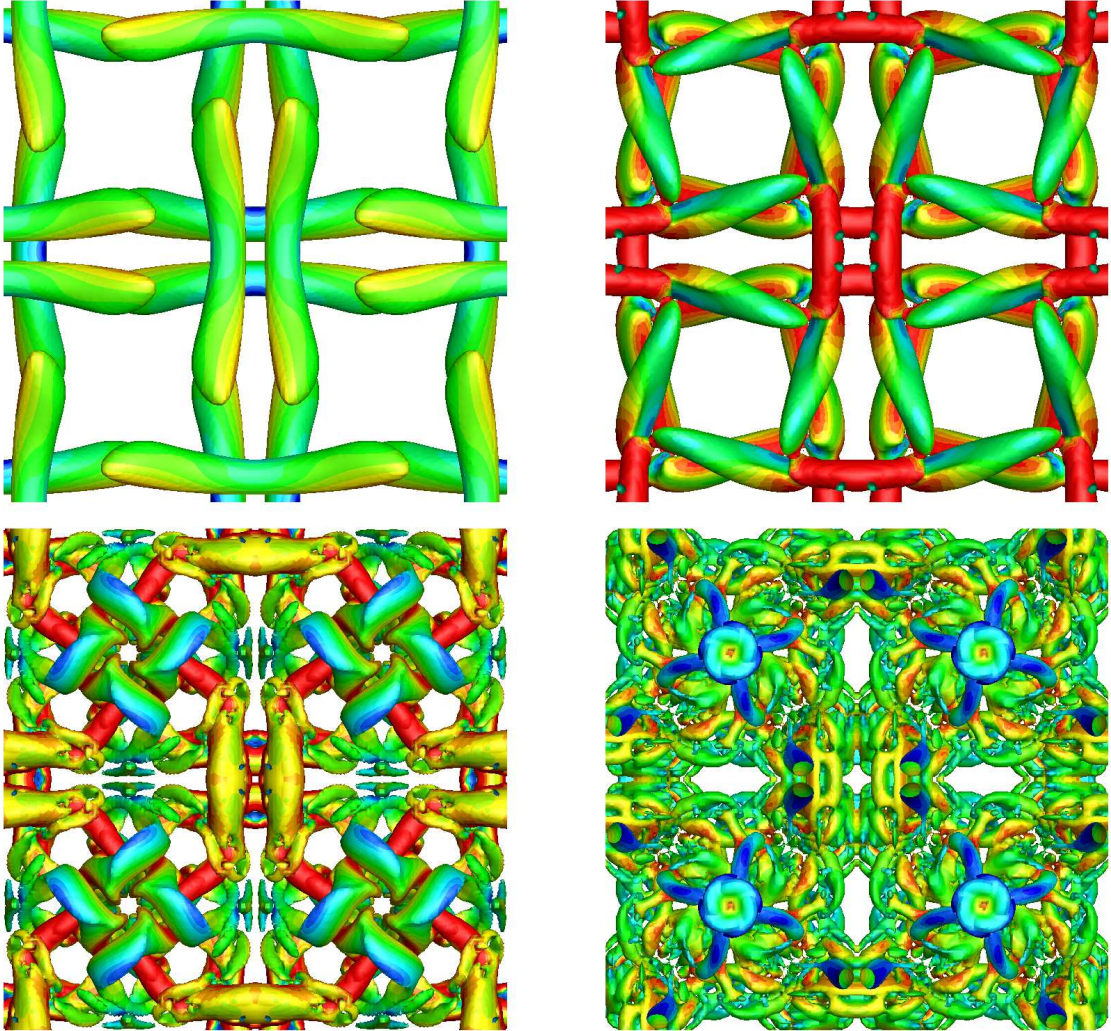


Figure 2: Taylor-Green vortex: iso-surface of the second invariant of velocity gradient tensor at $t = 2.5, 5, 7.5$ and 10 colored by velocity magnitude.

The volume-averaged kinetic energy is given by

$$E_k = \frac{1}{\rho_0 \Omega} \int_{\Omega} \frac{1}{2} \rho \mathbf{U} \cdot \mathbf{U} d\Omega,$$

where Ω is the volume of the computational domain. The dissipation rate of kinetic energy can be computed by the temporal derivative of E_k

$$\varepsilon(E_k) = -\frac{dE_k}{dt},$$

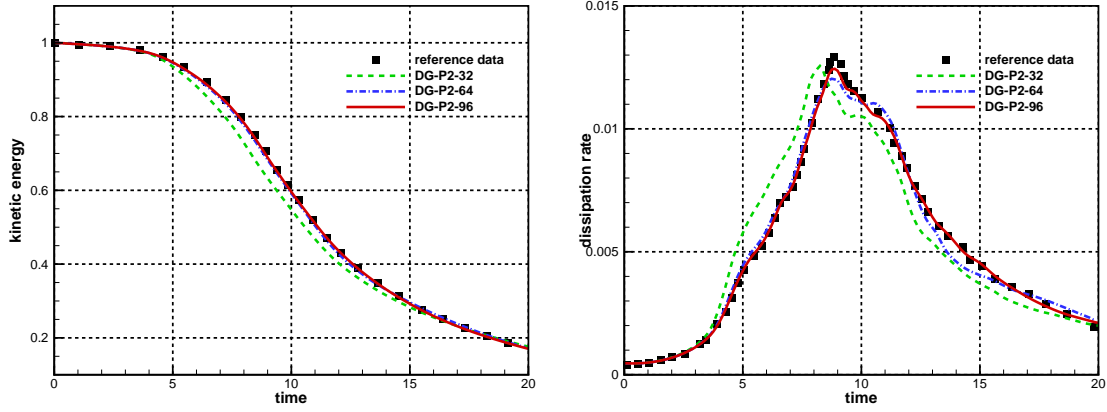


Figure 3: Taylor-Green vortex: the time history of kinetic energy (left) and dissipation rate (right) of DG-HGKS- \mathbb{P}_2 with 32^3 , 64^3 and 96^3 cells.

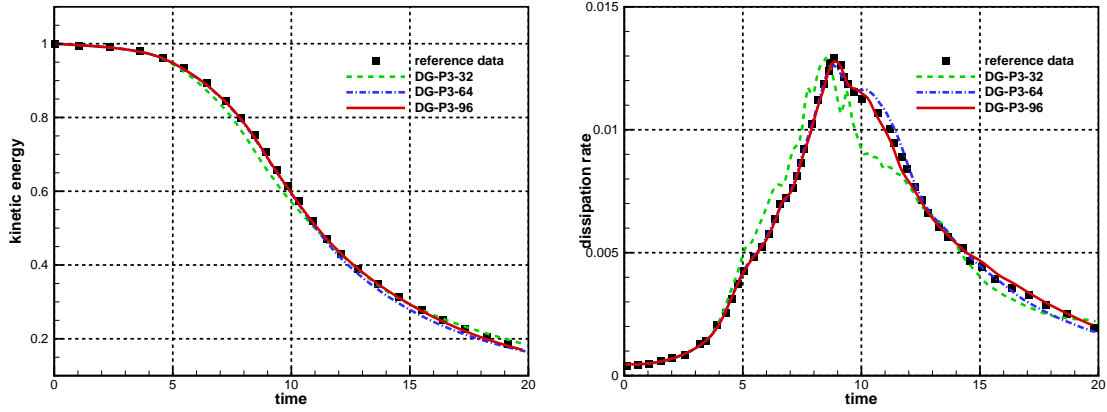


Figure 4: Taylor-Green vortex: the time history of kinetic energy (left) and dissipation rate (right) of DG-HGKS- \mathbb{P}_3 with 32^3 , 64^3 and 96^3 cells.

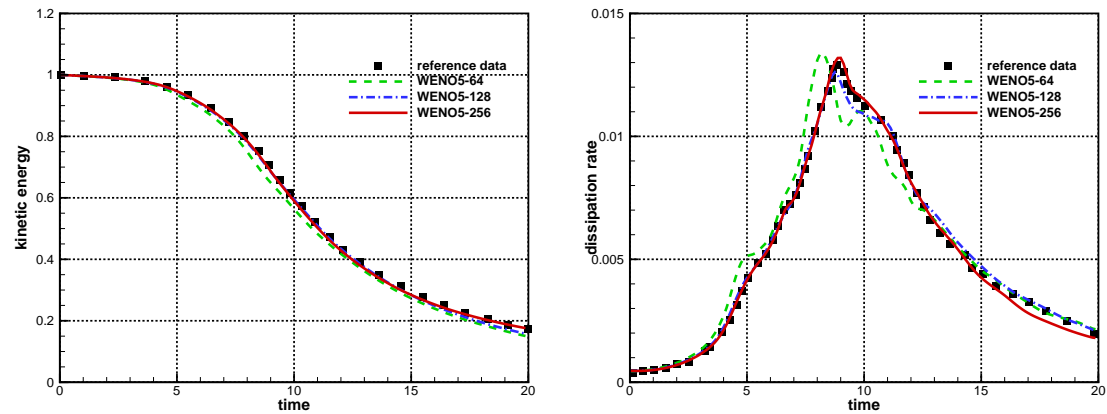


Figure 5: Taylor-Green vortex: the time history of kinetic energy (left) and dissipation rate (right) of WENO-HGKS with 64^3 , 128^3 and 256^3 cells.

which is computed by second order central difference in the numerical results of E_k . For the incompressible limit, the dissipation rate is related to the integrated enstrophy by

$$\varepsilon(\zeta) = \frac{2\mu}{\rho_0\Omega} \int_{\Omega} \frac{1}{2} \rho \boldsymbol{\omega} \cdot \boldsymbol{\omega} d\Omega,$$

where μ is the coefficient of viscosity and $\boldsymbol{\omega} = \nabla \times \mathbf{U}$. The numerical results of BB13 scheme [16, 4] are provided as reference data, where a high-order finite difference method equipped with fourth-stage third-order algorithm for time discretization and 13-point stencils for spatial discretization. The time histories of kinetic energy and dissipation rate of DG-HGKS- \mathbb{P}_2 and DG-HGKS- \mathbb{P}_3 and WENO methods are shown in Figure.3, Figure.4 and Figure.5, respectively. The reasonable agreements are observed with the reference solution, except for the results of DG schemes with 32^3 cells and WENO scheme with 64^3 cells. With the refinement of mesh, the DG-HGKS can capture the benchmark solution more accurately, which verifies the convergence of DG schemes. The dissipation rate is determined by both physical and numerical dissipation, and most of high-order schemes can resolve it well with a not very refine mesh. However, the integrated enstrophy is much more difficult to capture for all schemes. The time histories of integrated enstrophy are shown in Figure.6 for DG-HGKS- \mathbb{P}_2 and DG-HGKS- \mathbb{P}_3 . The magnitude of errors highly depends on the order of accuracy of the scheme. A large discrepancy is observed for the integrated enstrophy except for DG-HGKS- \mathbb{P}_3 using 96^3 cells. The comparisons with WENO scheme are given in Figure.7 for the integrated enstrophy. According to the quantitative analysis of numerical dissipation [24], the performance of the integrated enstrophy is sensitive to both numerical dissipation and degree of freedom (DoF) of high-order scheme. The DG-HGKS- \mathbb{P}_2 has 10 and DG-HGKS- \mathbb{P}_3 has 20 DoFs inside each cell. Meanwhile, the WENO-HGKS has only one DoF inside each cell. Due to the only third-order of accuracy, the performance of DG- \mathbb{P}_2 method with 96^3 cells are only comparable with WENO-HGKS with 128^3 cells, and a large discrepancy is also observed compared with the reference data. With the increase of DoF and order of accuracy, DG-HGKS- \mathbb{P}_3 performs much better than DG-HGKS- \mathbb{P}_2 . Due to the approximate number of DoF, the time history of integrated enstrophy of DG-HGKS- \mathbb{P}_3 with 96^3 cells are comparable with that of WENO-HGKS with 256^3 cells, and both of them agree well with the reference data. However, for the flow with discontinuities, such as the compressible isotropic turbulence with initial turbulent Mach number 0.5 and Taylor microscale Reynold number 72, WENO-HGKS works well even with linear weights, but the DG-HGKS fails without special treatment. The DG methods seem to lack robustness, and more great efforts need to be paid to the limiters and trouble cell indicators beforehand [33, 34].

The comparison of computational cost is also studied, where the detailed mesh size, time step, CFL number and CPU time for DG-HGKS and WENO-HGKS are presented in Table.14. The CPU time are computed per 10 steps for each method by Intel i7-9700 CPU using OpenMP directives. Unsurprisingly, due to the fewer Gaussian quadrature points of DG-HGKS- \mathbb{P}_2 , DG-HGKS- \mathbb{P}_2 is much more efficient DG-HGKS- \mathbb{P}_3 . With the same number of cells, no doubt that DG-HGKS is less efficient than WENO-HGKS. Taken the degree of freedom into account, the CPU time of WENO-HGKS with 256^3 cells is around 2.15

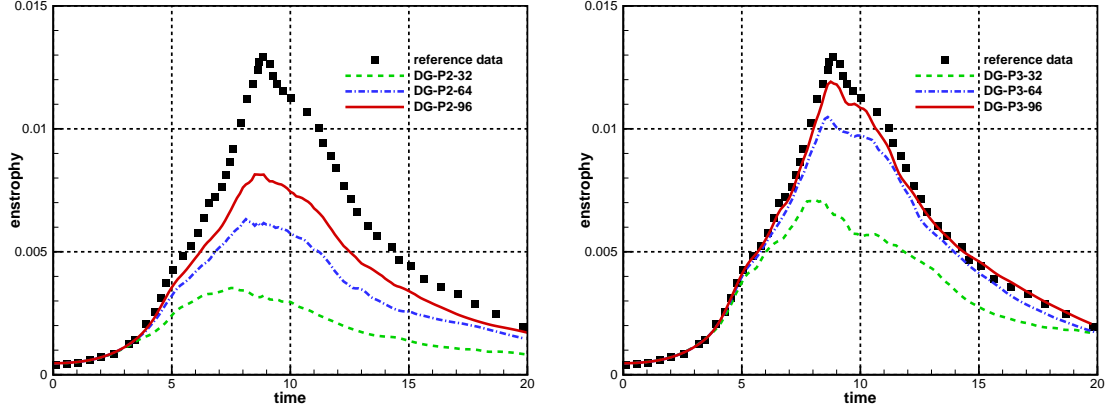


Figure 6: Taylor-Green vortex: the time history of integrated enstrophy for DG-HGKS- \mathbb{P}_2 (left) and DG-HGKS- \mathbb{P}_3 (right) with 32^3 , 64^3 and 96^3 cells.

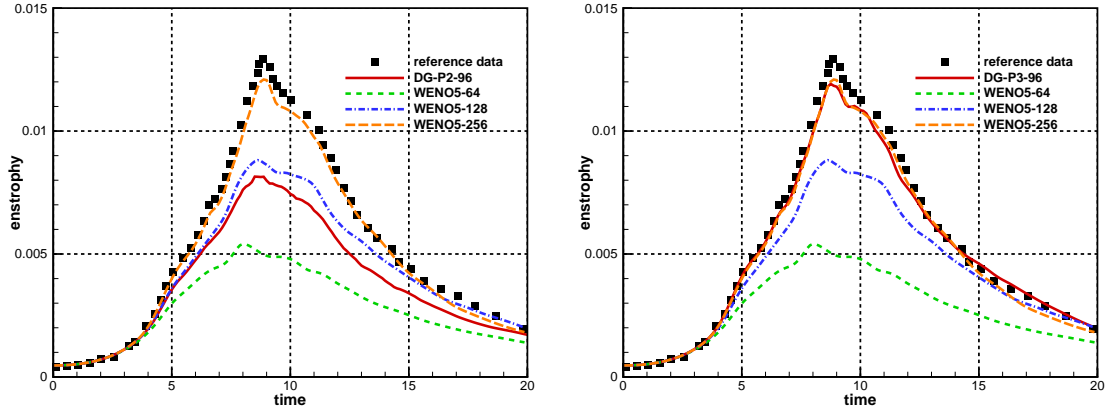


Figure 7: Taylor-Green vortex: the comparison of DG-HGKS- \mathbb{P}_2 , DG-HGKS- \mathbb{P}_3 and WENO-HGKS for time history of integrated enstrophy.

times of DG-HGKS- \mathbb{P}_3 with 96^3 cells. The CPU time of WENO-HGKS is around 1/1.66 of DG-HGKS- \mathbb{P}_3 . Thus, the total computational cost of WENO-HGKS is comparable with DG-HGKS- \mathbb{P}_3 . However, to improve the accuracy of DG scheme, much more quadrature points and numerical fluxes are needed, and much smaller time step is used, which cause the dramatical increase of computational cost for DG method.

method	mesh size	time step	CFL number	CPU time (per 10 steps)
DG- \mathbb{P}_2	96^3	8.86×10^{-4}	0.15	46s
DG- \mathbb{P}_3	96^3	5.35×10^{-4}	0.09	155s
WENO-5	256^3	8.92×10^{-4}	0.40	333s

Table 14: Taylor-Green vortex: comparison of efficiency for DG-HGKS and WENO-HGKS.

6. Conclusion

In this paper, the DG-HGKS is developed for the compressible Euler and Navier-Stokes equations. Different from the traditional DG approaches, the time dependent flux is provided by the gas-kinetic flow solver. In the framework of DG-HGKS, the inviscid and viscous fluxes can be calculated uniformly, which avoid the treatment of diffusion terms in LDG [14] and DDG [11] methods. Due to the time dependent numerical flux, the temporal accuracy is achieved by two-stage fourth-order discretization [26, 32]. With \mathbb{P}_2 and \mathbb{P}_3 elements, the third-order and fourth-order spatial accuracy can be achieved. In the computation, we mainly concentrate on the smooth flows, and numerical tests are presented to validate the performance of current scheme. The accuracy tests are presented to validate the optimal convergence and super-convergence for DG discretization with uniform and nonuniform meshes, and the Taylor-Green vortex are provided to validate the efficiency and accuracy for the nearly incompressible turbulence. The numerical results of WENO-HGKS are given as well. Both DG-HGKS and WENO-HGKS work well for the smooth flows. As expected, the numerical performances, including the resolution and efficiency, are comparable with the approximate number of degree of freedom. To accelerate the computation, the DG-HGKS is implemented to run on Nvidia GPUs using CUDA. Obtained results are compared with those obtained by Intel i7-9700 CPU using OpenMP directives. The GPU code achieves 6x-7x speedup with TITAN RTX, and 10x-11x speedup with Tesla V100. In the future, more challenging problems for compressible flows, such as the supersonic and hypersonic flat plate turbulent boundary layer, will be investigated.

Acknowledgement

This research is supported by National Natural Science Foundation of China (11701038), the Fundamental Research Funds for the Central Universities.

References

- [1] F. Bassi, A. Crivellini, D.A. Di Pietro, S. Rebay, An artificial compressibility flux for the discontinuous Galerkin solution of the incompressible Navier-Stokes equations, *J. Comput. Phys.* 218 (2006) 794-815.
- [2] F. Bassi, A. Crivellini, D.A. Di Pietro, S. Rebay, An implicit high-order discontinuous Galerkin method for steady and unsteady incompressible flows, *Comput. Fluids* 36 (2007) 1529-1546.
- [3] P.L. Bhatnagar, E.P. Gross, M. Krook, A Model for Collision Processes in Gases I: Small Amplitude Processes in Charged and Neutral One-Component Systems, *Phys. Rev.* 94 (1954) 511-525.
- [4] C. Bogey, C. Bailly, A family of low dispersive and low dissipative explicit schemes for flow and noise computations, *J. Comput. Phys.* 194 (2004) 194-214.
- [5] M.E. Brachet, D.I. Meiron, S.A. Orszag, B.G. Nickel, R.H. Morf, U. Frisch, Small-scale structure of the Taylor-Green vortex, *J. Fluid. Mech.* 130 (1983) 411-452.
- [6] J. R. Bull, A. Jameson, Simulation of the compressible Taylor-Green vortex using high-order flux reconstruction schemes, *AIAA* 2014-3210.
- [7] R. Borges, M. Carmona, B. Costa, W. S. Don, An improved weighted essentially non-oscillatory scheme for hyperbolic conservation laws, *J. Comput. Phys.* 227 (2008) 3191-3211.
- [8] G.Y. Cao, L. Pan, K. Xu, High-order gas-kinetic scheme with parallel computation for direct numerical simulation of turbulent flows, *J. Comput. Phys.* 448 (2022) 110739

- [9] W. Cao, C.-W. Shu, Y. Yang and Z. Zhang, Superconvergence of discontinuous Galerkin method for scalar nonlinear hyperbolic equations. *SIAM J. Numer. Anal.* 56 (2018) 732-765.
- [10] S. Chapman, T.G. Cowling, *The Mathematical theory of non-uniform gases*, third edition, Cambridge University Press, (1990).
- [11] J. Cheng, X.Q. Yang, X.D. Liu, T.G. Liu, H. Luo, A direct discontinuous Galerkin method for the compressible Navier–Stokes equations on arbitrary grids, *J. Comput. Phys.* 327 (2016) 484-502.
- [12] B. Cockburn, C.-W. Shu, TVB Runge-Kutta local projection discontinuous Galerkin finite element method for conservation laws II: General framework, *Math. Comput.* 52 (1989) 411-435.
- [13] B. Cockburn, C.-W. Shu, The Runge-Kutta discontinuous Galerkin method for conservation laws V: Multidimensional systems, *J. Comput. Phys.* 141 (1998) 199-224.
- [14] B. Cockburn, G. Kanschat, D. Schötzau, A locally conservative LDG method for the incompressible Navier-Stokes equations, *Math. Comput.* 74 (2005) 1067-1095.
- [15] B. Cockburn, S.Y. Lin, C.-W. Shu, TVB Runge-Kutta local projection discontinuous Galerkin finite element method for conservation laws III: One dimensional systems, *J. Comput. Phys.* 84 (1989) 90-113.
- [16] J. Debonis, Solutions of the Taylor-Green vortex problem using high-resolution explicit finite difference methods, *AIAA Paper* (2013) 2013-0382.
- [17] Z.F. Du, J.Q. Li, A Hermite WENO reconstruction for fourth order temporal accurate schemes based on the GRP solver for hyperbolic conservation laws, *J. Comput. Phys.* 355 (2018) 385-396.
- [18] H. Gao, Z.J. Wang, A high-order lifting collocation penalty formulation for the Navier-Stokes equations on 2D mixed grids, *AIAA Paper* (2009) 3784.
- [19] S. Gottlieb, C. W. Shu, Total variation diminishing Runge-Kutta schemes, *Mathematics of computation*, 67 (1998) 73-85.
- [20] A. Harten, B. Engquist, S. Osher and S. R. Chakravarthy, Uniformly high order accurate essentially non-oscillatory schemes, III. *J. Comput. Phys.* 71 (1987) 231-303.
- [21] H.T. Huynh, A flux reconstruction approach to high-order schemes including discontinuous Galerkin methods, *AIAA Paper* 2007 4079.
- [22] H.T. Huynh, Z.J. Wang, P.E. Vincent, High-order methods for computational fluid dynamics: A brief review of compact differential formulations on unstructured grids, *Computers & Fluids* 98 (2014) 209-220
- [23] X. Ji, L. Pan, W. Shyy , K. Xu, A compact fourth-order gas-kinetic scheme for the Euler and Navier-Stokes equations, *J. Comput. Phys.* 372 (2018) 446-472.
- [24] X. Ji, F.X. Zhao, W. Shyy, K. Xu, A family of high-order gas-kinetic schemes and its comparison with Riemann solver based high-order methods, *J. Comput. Phys.* 356 (2018) 150-173.
- [25] G.S. Jiang, C.-W. Shu, Efficient implementation of weighted ENO schemes, *J. Comput. Phys.* 126 (1996) 202-228.
- [26] J.Q. Li, Z.F. Du, A two-stage fourth order time-accurate discretization for Lax-Wendroff type flow solvers I. hyperbolic conservation laws, *SIAM J. Sci. Computing*, 38 (2016) 3046-3069.
- [27] H.L. Liu, J. Yan, The direct discontinuous Galerkin (DDG) methods for diffusion problems, *SIAM J. Numer. Anal.* 47 (2009) 675-698.
- [28] X.D. Liu, S. Osher, T. Chan, Weighted essentially non-oscillatory schemes, *J. Comput. Phys.* 115 (1994) 200-212.
- [29] Y. Liu, M. Vinokur, Z. J. Wang, Spectral difference method for unstructured grids I: Basic formulation, *J. Comput. Phys.* 216 (2006) 780-801.
- [30] H. Luo, L.Q. Luo, R. Nourgaliev, V.A. Mousseau, N. Dinh, A reconstructed discontinuous Galerkin method for the compressible Navier-Stokes equations on arbitrary grids, *J. Comput. Phys.* 229 (2010) 6961-6978.
- [31] X. Meng, C.-W. Shu, B. Wu, Optimal error estimates for discontinuous Galerkin methods based on upwind-biased fluxes for linear hyperbolic equations. *Math. Comput.* 85 (2016) 1225-1261.
- [32] L. Pan, K. Xu, Q.B. Li, J.Q. Li, An efficient and accurate two-stage fourth-order gas-kinetic scheme for the Navier-Stokes equations, *J. Comput. Phys.* 326 (2016) 197-221.
- [33] J. X. Qiu, C.-W. Shu, Hermite WENO schemes and their application as limiters for Runge–Kutta

- discontinuous Galerkin method: one dimensional case, *J. Comput. Phys.* 193 (2003) 115-135.
- [34] J.X. Qiu, C.-W. Shu, Runge–Kutta discontinuous Galerkin method using WENO limiters, *SIAM Journal on Scientific Computing* 26 (2005) 907-929.
 - [35] W.H. Reed, T.R. Hill, Triangular mesh methods for the neutron transport equation, Los Alamos Scientific Laboratory Report, LA-UR-73-479 (1973).
 - [36] X.D. Ren, K. Xu, W. Shyy, C.W. Gu, A multi-dimensional high-order discontinuous Galerkin method based on gas kinetic theory for viscous flow computations, *J. Comput. Phys.* 292 (2015) 176-193.
 - [37] C.-W. Shu, S. Osher, Efficient implementation of essentially non-oscillatory shock capturing schemes, *J. Comput. Phys.* 77 (1988) 439-471.
 - [38] E.F. Toro, *Riemann Solvers and Numerical Methods for Fluid Dynamics*, Third Edition, Springer (2009).
 - [39] Z.J. Wang, Spectral (finite) volume method for conservation laws on unstructured grids: basic formulation, *J. Comput. Phys.* 178 (2002) 210-251.
 - [40] C.F. Xu, X.G. Deng, et al., Collaborating CPU and GPU for large-scale high-order CFD simulations with complex grids on the TianHe-1A supercomputer, *J. Comput. Phys.* 278 (2014) 275-297.
 - [41] K. Xu, *Direct modeling for computational fluid dynamics: construction and application of unified gas kinetic schemes*, World Scientific (2015).
 - [42] K. Xu, A gas-kinetic BGK scheme for the Navier-Stokes equations and its connection with artificial dissipation and Godunov method, *J. Comput. Phys.* 171 (2001) 289-335.
 - [43] K. Xu, Discontinuous Galerkin BGK method for viscous flow equations: One-dimensional systems. *Siam J. Sci. Comput.* 25 (2004) 1941-1963.